# Distinct point defect behaviours in body-centered cubic medium-entropy alloy NbZrTi induced by severe lattice distortion

Tan Shi [a], Zhengxiong Su [a], Jing Li [a], Chenguang Liu [c], Jinxue Yang [a], Xinfu He [d], Di Yun [a], Qing Peng [e,*], Chenyang Lu [a,b,**]

[a] School of Nuclear Science and Technology, Xi'an Jiaotong University, Xi'an, 710049, China
[b] State Key Laboratory of Multiphase Flow in Power Engineering, Xi'an Jiaotong University, Xi'an, 710049, China
[c] College of Nuclear Equipment and Nuclear Engineering, Yantai University, Yantai, 264005, China
[d] China Institute of Atomic Energy, Beijing, 102413, China
[e] State Key Laboratory of Nonlinear Mechanics, Institute of Mechanics, Chinese Academy of Sciences, Beijing, 100190, China

## ARTICLE INFO

## ABSTRACT

The point defect properties of body-centered cubic medium-entropy alloy NbZrTi were studied by first-principles calculations. Due to severe lattice distortion, a significant portion of conventional vacancy and interstitial structures are unstable and require large structural relaxation, indicating an irregular energy landscape with large site-to-site variations. The average vacancy and interstitial formation energy are 0.95 eV$\pm$ 0.34 eV and 1.92 eV $\pm$ 0.39 eV, respectively, much lower than that of Nb (2.77 eV and 4.38 eV). The vacancy migration energy exhibits a wide distribution extending to 0 eV, resulting in preferential vacancy migration through low barrier sites. The interstitial diffusion is slower than that of pure Nb due to the reduction of long <111> diffusion induced by the site-to-site variations in stable interstitial orientations. Ti atoms diffuse much faster than Nb and Zr atoms due to the preferential interstitial binding with Ti. The effect of atomic composition and short-range order on elemental and total interstitial diffusion was also investigated. The obtained first-principles results are important for the development of interatomic potentials for radiation damage studies. When irradiated with 3-MeV Fe ions at 675 °C to a peak dose of ∼100 dpa, NbZrTi reduced the void formation at high temperature compared to Nb owing to its higher equilibrium vacancy concentration and closer mobility between vacancies and interstitial atoms.

© 2022 Acta Materialia Inc. Published by Elsevier Ltd. All rights reserved.

## 1. Introduction

Medium-entropy alloys (MEAs) and high-entropy alloys (HEAs) are important groups of multi-principal element alloys (MPEAs), a class of materials with two or more principal alloying elements. The entropy-based definitions originate from the contribution of high mixing entropy to the formation of solid-solution phase [1]. MPEAs have demonstrated excellent mechanical properties [2,3] and damage resistance [4] owing to their unique features of lattice distortion, sluggish diffusion, high-entropy effect and cocktail effect [1]. Among MPEAs, MEA NbZrTi and NbZrTi-based refractory HEAs have exhibited great mechanical performance and have shown great promise for applications as high-temperature structural materials [3,5,6]. This group of materials

has been recently considered for potential employment in advanced nuclear reactors [7]. The advanced reactors pose severe challenges to the material performance, as materials need to suffer from high operating temperature (up to 1050 °C), high irradiation damage (up to 150 displacement per atom (dpa)), harsh corrosive environment, and also ideally a longer service time [8,9]. Therefore, there is a continuous demand for ideal material candidates that can meet these extreme requirements. As conventional refractory alloys, NbZrTi-based refractory MPEAs have excellent mechanical strength at high temperature [3]. In addition, various types of NbZrTi-based alloys have also shown good room-temperature ductility [7], such as NbZrTi [5], NbZrTiHf [10], NbZrTiHfTa [11,12], NbZrTiMo$_{0.3}$V$_{0.3}$ [13], NbZrTiTaHfMo$_{0.75}$ [14], (NbZrTiHf)$_{0.95}$Al$_{0.05}$ [15], etc. The body-centered cubic (BCC) structure also has an intrinsically better resistance to radiation-induced void swelling [16]. The concept of MPEAs offers a large compositional space for the material property tuning, but the actual application of a material is usually a multifaceted problem where different properties need to be balanced at the stage of alloy design. While the aspects of alloy production and mechanical properties of vari-

* Corresponding author.
** Corresponding author at: School of Nuclear Science and Technology, Xi'an Jiaotong University, Xi'an, 710049, China.
E-mail addresses: pengqing@imech.ac.cn (Q. Peng), chenylu@xjtu.edu.cn (C. Lu).

ous alloy compositions have been studied previously [3], the point defect properties have rarely been explored. As point defect energetics have a great impact on the mechanical properties [17], corrosion behaviours [18] and radiation resistance [19], they are studied in this work with NbZrTi as a representative material to show the distinct point defect properties of this group of materials.

Point defect behaviours have been systematically studied in face-centered cubic (FCC) structures, including Ni-based binary and ternary MPEAs [19,20], Co-free HEA NiFeMnCr [21] and CoCrNi-based MPEAs [22], and have also been studied in BCC HEA VTaCrW [23]. These studies have all shown that point defect formation and migration energies exhibit a certain degree of energy fluctuation due to the difference in the local chemical environment, and the interstitial diffusion is reduced due to lattice distortion and sluggish diffusion effect. The closer mobility between vacancies and interstitials is believed to promote the point defect recombination during irradiation. However, the defect energy seems to be also alloy dependent. For example, there is no consistent trend for the relative magnitude of vacancy formation energy compared to the constituent elements. In addition, due to the more severe lattice distortion of BCC MPEAs, the energy distribution is much wider [23], indicating significantly different point defect properties from their widely studied FCC counterparts.

Recently, there have been controversies regarding the currently established theory on the radiation resistance of MPEAs. FCC MPEAs, which are more extensively studied, have shown great radiation resistance including reduced void swelling [4,24], delayed defect microstructure growth and less degree of radiation-induced segregation [25]. It is believed to be attributed to the enhanced point defect recombination, slower energy dissipation, extended incubation period of dislocation loop growth and slower diffusion of defect clusters [4,20,25,26]. However, Parkin et al. found similar saturation dose for defect clusters between BCC NbTaTiV and V under heavy ion irradiation [27]. If the defect recombination rate is higher and the defect cluster growth is delayed, the threshold dose should be higher in MPEAs. The same work also showed that NbTaTiV with a large lattice distortion did not lead to a greater reduction in defect generation compared to its FCC counterparts, whereas the reduction in defect mobility is usually believed to be associated with the magnitude of lattice distortion. In addition, by the same method of molecular dynamics (MD) simulations of collision cascades induced by energetic particles [28], discrepancies exist on whether enhanced point defect recombination during the initial displacement cascade is a major contributor to the radiation resistance of MPEAs, which may be only caused by defect evolution on a longer time scale [29,30]. Recently, there has been great progress in the development of interatomic potentials for defect and radiation damage studies for BCC MPEAs, including MoNbTaVW [31], TiVTa [32,33] and VTaW [33]. Thus, for NbZrTi-based MPEAs and also other BCC MPEAs, it is crucial to first understand their unique point defect behaviours by first-principles method so that accurate interatomic potentials can be constructed and their impact on radiation resistance can be accurately characterized.

In this work, we present a first-principles investigation on the energy properties and migration behaviours of point defects in NbZrTi. First, the magnitude of lattice distortion of NbZrTi was characterized, showing more severe lattice distortion compared to FCC and some BCC MPEAs. Next, vacancy formation energy and migration energy were systematically calculated, revealing an unusual energy landscape induced by the large lattice distortion and chemical complexity. The interstitial formation energy and migration behaviours were then studied, along with the impact of atomic composition and short-range order (SRO) on interstitial migration. The obtained first-principles results were then used to benchmark an interatomic potential based on the embedding-atom method (EAM) potential. Ion irradiation experiment was performed at 675 °C with 3-MeV Fe ions at a peak dose of ~100 dpa to study the difference in radiation damage behaviours between pure Nb and NbZrTi, showing a direct impact of point defect energetics on the material irradiation resistance.

## 2. Methodology

### 2.1. First-principles calculations

The first-principles calculations were performed with the Vienna ab initio simulation package (VASP) using the projector-augmented wave method [34]. The generalized gradient approximation of Perdew-Burke-Ernzerhof (PBE) formalism was used to describe the exchange-correlation functionals [35]. Semi-core electrons were included in all calculations to describe short interatomic distances for interstitial configurations, where 13, 12 and 12 electrons were considered for Nb, Zr and Ti, respectively. The studied system consists of 128 atoms with 42 Nb atoms, 43 Zr atoms, and 43 Ti atoms. The alloy structure was constructed by the special quasi-random structure (SQS) method [36] using the Alloy Theoretic Automated Toolkit [37,38] to ensure the equal probability of appearance of each type of atom at the first nearest neighbour (1NN) and second nearest neighbour (2NN) sites. The Brillouin zone was sampled with a Monkhorst-Pack mesh of $3 \times 3 \times 3$. This choice of k-point grid was validated by vacancy and interstitial formation energies of pure Nb, Zr and Ti (see Fig. S1 of the Supplementary Materials for the comparison of vacancy and interstitial formation energies with different k-point meshes) [39–41]. The cutoff energy for the plane-wave basis was set to 400 eV, and the convergence criteria for ionic relaxation and self-convergence loop were set to $10^{-4}$ eV and 0.01 eV/Å, respectively. The spin polarization was initially included by using three different initial magnetic moments, but no magnetism was manifested after energy minimization. Thus, spin polarization was not included for all the following calculations of NbZrTi.

First, the system volume and atomic coordinates of the perfect lattice structure was determined based on the conjugate gradient optimization. The phonon calculation was performed to verify the structural dynamical stability. Second-order force constants of the supercell were calculated with a finite atomic displacement of 0.01 Å to each atom of the supercell for a total 768 sets of displacement. We maintained a k-point mesh of $3 \times 3 \times 3$ and used an additional support grid for the calculation of augmentation charges. The energy convergence criteria was set to $10^{-7}$ eV. The band unfolding method from Ref. [42,43] was used to decompose the phonon modes onto the Brillouin zone of the primitive BCC cell based on the crystallographic symmetry using the PHONOPY package [44].

Next, different vacancy and interstitial structures were constructed and relaxed with a fixed system volume. For the calculation of vacancy formation energies, 15 vacancies of each type of atom were randomly selected while it was ensured that the average number of each element is approximately equal at neighbouring sites. The initial structures for the calculation of interstitial formation energies include in total 18 <110> dumbbells, 18 <111> dumbbells, 9 <100> dumbbells and 9 tetrahedral sites with equal number of Nb, Zr or Ti atoms being added as the interstitial atoms. The choice of initial interstitial structures is based on the relative stability of different interstitial structures in pure Nb. Our simulations show that the final interstitial structures have weak dependence on the initial structures. In addition to the random generation of interstitial sites, different <110> and <111> dumbbell orientations at the same interstitial site was also simulated to study the impact of local chemical environment. The point defect forma-

tion energy was calculated as:

$$E_{def}^f = E_{def} - E_{per} \pm \mu_x, \tag{1}$$

where $E_{per}$ is the energy of the perfect structure, $E_{def}$ is the system energy with a vacancy/interstitial, and $\mu_x$ is the chemical potential of the removed atom (+) or added atom (-). The chemical potential of each element was determined by the Widom-type substitution technique [45] as adopted by previous defect studies of MPEAs [20,21]. By substituting one element to another and calculating the energy difference of the two systems, the chemical potential of each element can be determined. 20 substitutions were computed in total and the chemical potentials for Nb, Zr and Ti were determined to be -10.18 eV ± 0.03 eV, -8.39 eV ± 0.04 eV and -7.76 eV ± 0.02 eV, respectively. The Bader charge analysis was performed to determine the charge and volume of the removed atom [46].

The vacancy migration energies were computed using the climbing-image nudged elastic band (CI-NEB) method with a force convergence tolerance of 0.03 eV/Å [47]. In total, 60 migration paths were computed in which the first 30 migration paths used 3 or 5 intermediate images to characterize the shape of the migration barriers and the rest of the migration paths used 1 intermediate image to increase the statistics of the average migration energy. As there is a large variation among migration barriers of different sites, one intermediate image has sufficient accuracy to evaluate the average migration energy.

The interstitial migration dynamics behaviours were studied by the *ab initio* molecular dynamics (AIMD) method. In dynamics simulations, a single k-point was employed with an energy cutoff of 400 eV for the plane-wave basis. A systematic comparison of point defect formation energies was performed between a k-point mesh of $1 \times 1 \times 1$ and $3 \times 3 \times 3$, showing similar average formation energies and correct order for different types of interstitial pairs (see Table S1 and S2 of the Supplementary Materials for the comparison of vacancy and interstitial formation energies). The system was controlled by the NVT ensemble using the Nose-Hoover thermostat. The interstitial migration of different structures was compared at a temperature of 1200 K. The results were averaged over four different simulations in which the interstitial atom was introduced at a random site. For each simulation, after an initial equilibration time of 3 ps, a total simulation time of 32 ps was computed with a timestep of 2 fs. The mean square displacement (MSD) was analyzed by the VASP analysis program VASPKIT [48]:

$$MSD(m) = \frac{1}{N_a} \sum_{i=1}^{N_a} \frac{1}{N_t - m} \sum_{k=0}^{N_t - m - 1} (\mathbf{r}_i(k+m) - \mathbf{r}_i(k))^2, \tag{2}$$

where $m$ is the length of the time window, $\mathbf{r}_i(k)$ is the position vector of atom $i$ at a timestep of $k$, $N_t$ is the total number of timesteps, and $N_a$ is the total number of atoms. The MSD of the first half of the simulation time was selected to avoid large statistical variations at longer time due to limited integration timestep [19,49]. The interstitial trajectory was analyzed via the Wigner-Seitz defect analysis from the Ovito program [50]. The distribution of atomic positions of the perfect lattice was also studied with similar settings using the AIMD method at 300 K, 600 K and 900 K. The NVT ensemble was employed with a timestep of 3 fs for a total of 15 ps. The atom positions after 1000 timesteps were used to ensure the equilibration of the system.

Lattice Monte Carlo (MC) simulations were performed to obtain the SRO structure of NbZrTi [51]. The positions of two random atoms of different species were exchanged with an acceptance probability based on the Metropolis-Hastings sampling [52]. The applied temperature was 500 K. The supercell volume was optimized every 50 swaps. A k-point mesh of $1 \times 1 \times 1$ was used during the MC process. The Warren-Cowley SRO parameter was used
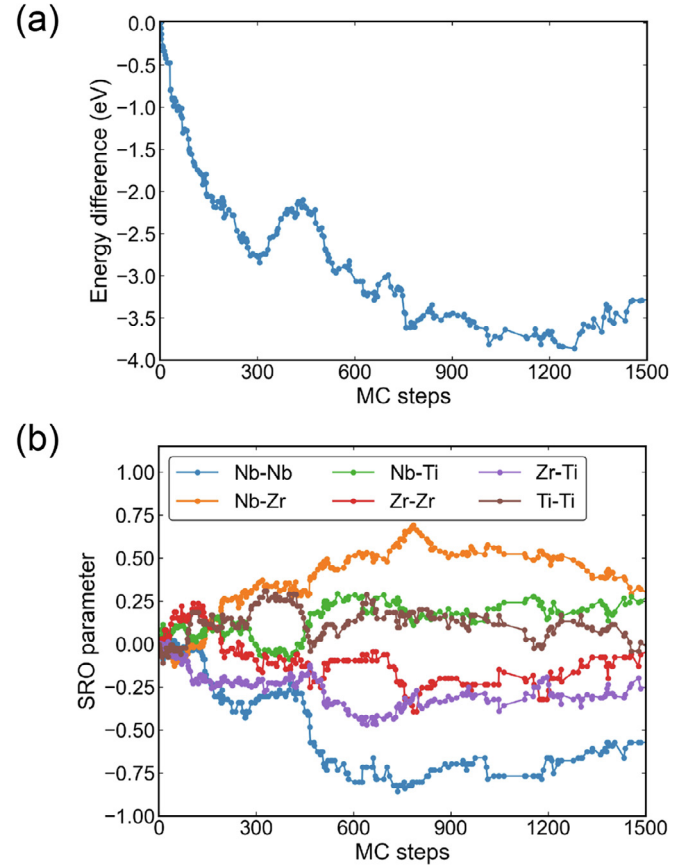


**Fig. 1.** (a) Evolution of accepted total energy relative to the initial system energy as a function of the Monte Carlo steps. (b) Evolution of Warren-Cowley SRO parameters of different atom pairs in the first nearest neighbour shell for the accepted Monte Carlo steps.

to describe the extent of chemical ordering [51,53]:

$$\alpha_{ij}^v = 1 - \frac{p_{ij}^v}{c_j}, \tag{3}$$

where $p_{ij}^v$ is the probability of finding element $j$ around element $i$ in the $v$th neighbouring shell, $c_j$ is the atomic concentration of element $j$. A random solid solution corresponds to a SRO parameter of zero. Positive and negative values correspond to a tendency of deceasing and increasing the number of $i, j$ pairs, respectively. As shown in Fig. 1, with the increase of MC steps, there is a general trend of energy decrease and a clear tendency of elemental ordering. Although it is difficult to obtain a full convergence with limited MC steps, the variations of system energy and SRO parameters become more gentle around 1500 steps. Thus, the SRO structure at 1500 MC steps was used for the following study of interstitial migration.

For comparison among BCC and FCC structures, equiatomic NiCoCr and NiCoFeCrMn with a FCC structure and equiatomic VTaTi and VTaW with a BCC structure were also studied by first-principles calculations with similar simulation settings. NiCoCr, VTaTi and VTaW were used to compare the extent of lattice distortion and NiCoFeCrMn was used to study the process of vacancy structural relaxation. For FCC structures, a supercell of 108 atoms was constructed with the SQS method. A Monkhorst-Pack grid of $2 \times 2 \times 2$ was used to sample the Brillouin zone with an energy cutoff of 500 eV for the plane-wave basis. Spin polarization was considered for all calculations to account for the magnetic properties of the constituent elements. For each alloy system, three dif-
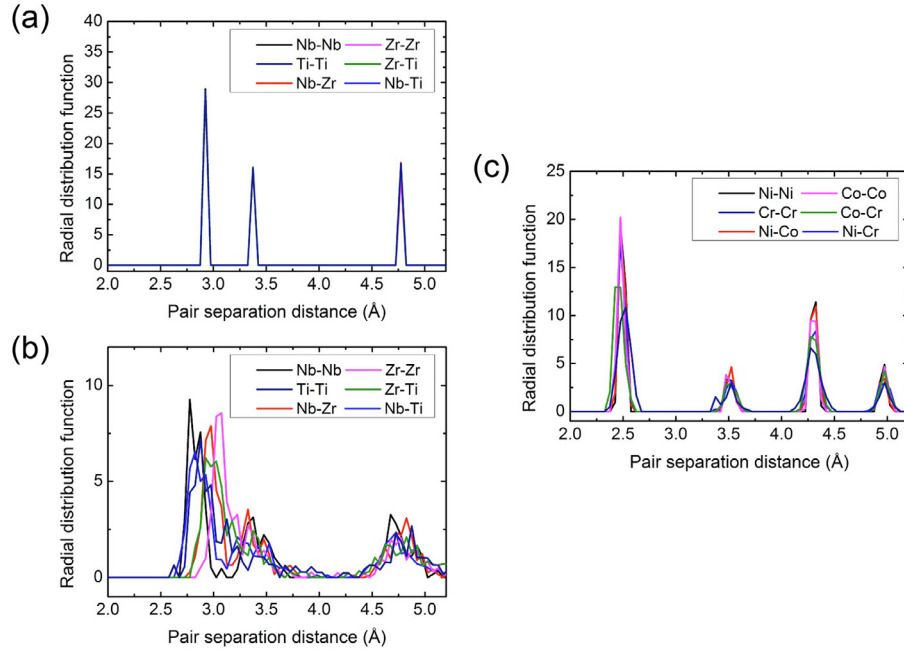
**Fig. 2.** Radial distribution function of the BCC NbZrTi structure constructed by the special quasi-random structure method (a) before and (b) after structural relaxation. The distributions from different atom pairs are overlapped in (a). (c) Radial distribution function of the FCC equiatomic NiCoCr alloy after structural relaxation.

ferent initial paramagnetic spin moments were considered, and the relaxed structure with the lowest system energy was selected.

### 2.2. Irradiation experiment and characterization

The NbZrTi with a nominal composition of $Nb_{33}Zr_{34}Ti_{33}$ (at.%) was prepared by arc melting and casting by mixing pure metals (purity > 99.9 wt.%) in a vacuum induction furnace. The as-cast alloys were homogenized at 1200 °C for 2 h in an Ar atmosphere to achieve a uniform elemental distribution. The as-homogenized bulk sample presented a single BCC structure, as evidenced by the X-ray diffraction pattern (see Fig. S2 of the Supplementary Materials). For comparison, Nb with a purity > 99.99 wt.% was also prepared for the irradiation experiment. Before irradiation, all samples were mechanically polished using colloidal silica and then vibratory polished to remove the stress layer, resulting in a mirror surface with a roughness of less than 3 nm. Subsequently, the samples were irradiated at 675 °C with 3-MeV Fe ions at a fluence of $1.02 \times 10^{17}$ ions/cm$^2$. The depth profile of displacement damage was calculated by the SRIM code [54], assuming a displacement threshold energy of 60 eV, 40 eV and 30 eV for Nb, Zr and Ti, respectively [55]. The peak dose was calculated to be 99.8 dpa and 129 dpa for Nb and NbZrTi, respectively, with the Kinchin-Pease option in the quick calculation mode [56].

After irradiation, a focused ion beam (FIB) lift-out technique was utilized to prepare the cross-sectional transmission electron microscope (TEM) samples. The FIB-induced damage was completely removed from the TEM samples using "flashing polishing" technique to avoid artifacts [57]. The characterization of radiation-induced defect microstructures was carried out on a FEI Talos-F200X operated at 200 kV.

## 3. Results

### 3.1. Local lattice distortion

Local lattice distortion is one of the important properties of MPEAs, which has a significant impact on their mechanical

**Table 1**
Quantification of the local lattice distortion in NbZrTi. The atomic radii are taken from Ref. [62].

| Atomic size mismatch $\delta$ (%) | Local atomic distortion parameter $\alpha_2$ | Average atomic displacement $\Delta d$ (Å) |
|---|---|---|
| 5.03 | 0.023 | 0.171 |

properties, electrical and thermal conductivity, and damage tolerance [4,58,59]. Based on first-principles calculations, the lattice constant for NbZrTi is 3.381 Å, which is in good agreement with experimental results of 3.36 – 3.41 Å [5]. The BCC HEAs tend to have a larger lattice distortion than FCC NiCoFeCrMn-based alloys due to the larger atomic size mismatch [60,61]. It is shown from Fig. 2(b) and (c) that after structural relaxation, the broadening in the atomic distance is much wider in NbZrTi than the FCC MEA NiCoCr. Severe lattice distortion can be seen by the overlap between the 1NN and 2NN in the radial distribution function, which is also seen in other refractory MEAs and HEAs including VTaCrW, HfNbZr, HfNbTiZr and HfNbTaTiZr [23,61].

The extent of lattice distortion of NbZrTi is quantified here by several commonly used parameters [60,61,63], as listed in Table 1:

$$\delta = \sqrt{\sum_i^n c_i (1 - r_i/\bar{r})^2}, \ \bar{r} = \sum_i^n c_i r_i, \tag{4}$$

$$\alpha_2 = \sum_{j \geq i}^n \frac{c_i c_j |r_i + r_j - 2\bar{r}|}{2\bar{r}}, \tag{5}$$

$$\Delta d = \frac{1}{N_a} \sum_i |\mathbf{r}_{\text{relaxed},i} - \mathbf{r}_{\text{unrelaxed},i}|, \tag{6}$$

where $r_i$ and $c_i$ are the atomic radius and atomic percentage of element $i$, $\mathbf{r}_{\text{unrelaxed}}$ and $\mathbf{r}_{\text{relaxed}}$ are atomic position vectors in unrelaxed and relaxed structures, $N_a$ is the total number of atoms, and $\alpha_2$ adopts the parameter representation from Ref. [60] to reflect the pairwise relationship between different atom types. $\delta$ is
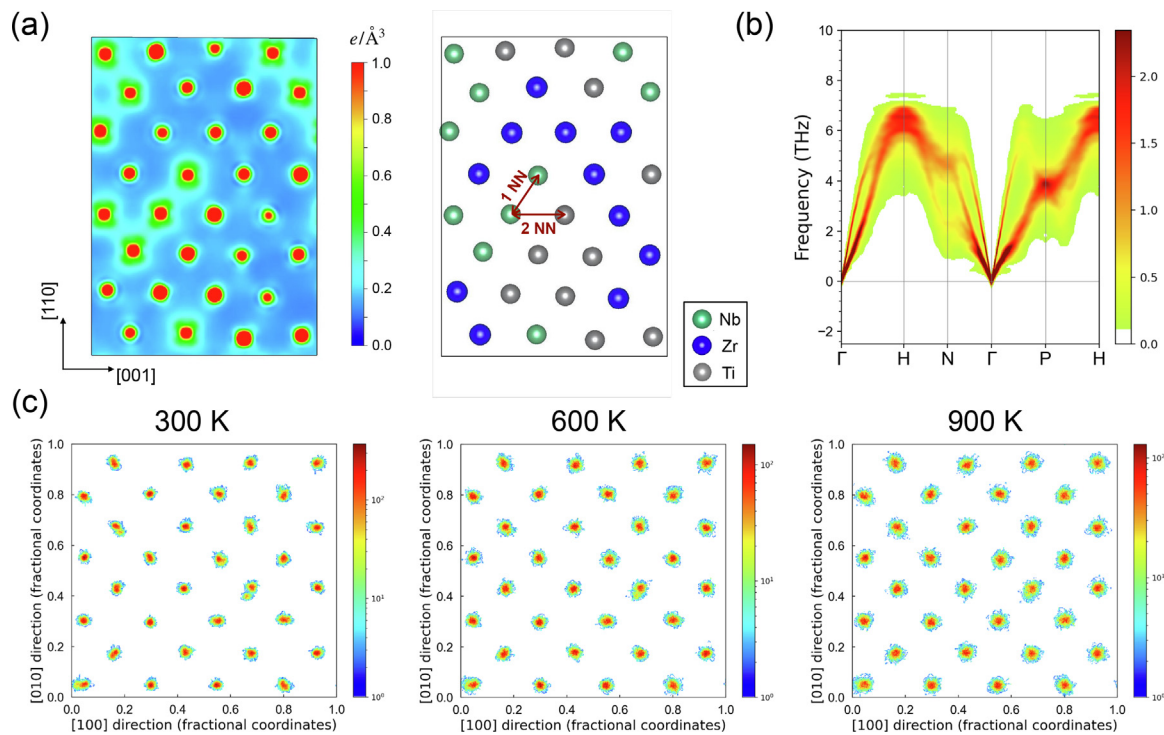
**Fig. 3.** (a) Valence charge density of NbZrTi and the corresponding atom types in the $(1\bar{1}0)$ plane. The partial charge density from $E_f$ - 5 eV to $E_f$ was selected, where $E_f$ is the Fermi energy. (b) Phonon band spectrum of NbZrTi. (c) Spatial distribution of atomic positions of NbZrTi at a temperature of 300 K, 600 K and 900 K. Atom positions at each timestep are projected in the (001) plane with four atoms aligned in the same column.

frequently used to estimate the lattice distortion due to the atomic size difference [63,64], and $\alpha_2$ has shown strong correlation with different alloy properties including phase, intrinsic elastic strain energy and excess entropy [60]. However, these two parameters are calculated directly from the elemental radii, whereas $\Delta d$ is determined by the first-principles method, which should provide a more accurate measure of the lattice distortion. The parameter of $\Delta d$ was compared among supercells of different sizes, showing that a supercell of 128 atoms is sufficient to represent the lattice distortion (see Fig. S3 of the Supplementary Materials for the comparison of supercell sizes of 54 atoms, 128 atoms and 250 atoms). The $\Delta d$ parameters for Nb, Zr and Ti are 0.14 Å, 0.15 Å and 0.22 Å, respectively, where Ti has the largest displacement from its ideal lattice site.

By examining the 1NN bond length of different atom pairs, it is shown that Zr atoms tend to have larger bond length while Nb-containing bond length tends to be smaller. Ti atom, as the lightest element in NbZrTi, tends to accommodate these differences by atomic displacements. By analyzing the projected density of states (DOS) of different elements, it is also shown that Ti has a large DOS near Fermi level, which generally suggests its inferior lattice instability compared to Nb and Zr [23,65]. Thus, large relaxation can further help stabilize Ti atoms in the BCC structure. The supporting evidence related to bond length and DOS analysis can be found in Table S3, Fig. S4 and Fig. S5 of the Supplementary Materials. In addition, there is a tendency of forming larger atomic displacement when there are fewer Nb atoms in the 1NN. The $d$-orbitals of a BCC structure can be classified into the $d - e_g$ and $d - t_{2g}$ component. The $d - t_{2g}$ contribution points along the <111> direction (direction of 1NN) and helps stabilize the BCC structure, whereas the $d - e_g$ contribution points along the <100> direction (direction of 2NN) [66]. The valence charge density of NbZrTi is presented in Fig. 3(a) in the $(1\bar{1}0)$ plane to visualize both 1NN and 2NN chemical bonding. Clearly, Nb atoms have a strong $d - t_{2g}$ component along the <111> direction, which is manifested

by the higher charge density between nearest neighbours. In contrast, the 1NN bonding is relatively weaker for Ti and Zr atoms. Thus, when fewer Nb atoms are present in the surroundings, especially with 0 or 1 Nb atom in the 1NN, the lack of stabilizing element leads to larger local lattice distortion.

Although local lattice distortion has proved to be essential in stabilizing BCC structures [67,68], atomic displacements from chemically-induced lattice distortion could be intermixed with atomic displacements induced by the tendency of structural transformation [68]. Thus, before performing systematic defect calculations, the phonon dispersion of the perfect lattice was calculated, as shown in Fig. 3(b). Below zero frequency, there is little imaginary component (less than 0.05 THz$^{-1}$ in the spectral function), showing the stability of the studied structure. Significant phonon broadening can be observed due to the fluctuations of mass and force constant in the MPEAs and the extent of broadening is also consistent with other refractory MPEAs [43]. As the structural instability is usually associated with the transition to HCP and $\omega$ phases, three HCP and $\omega$ phase SQS structures were constructed using 96 atoms and 81 atoms, respectively. If the cell shape was not fixed, all six configurations relaxed to BCC structure after energy minimization (see Fig. S6 of the Supplementary Materials for the structural transformation). If the cell shape was fixed, the energy of HCP phase was 33 meV/atom higher than the BCC phase, whereas the $\omega$ phase still transformed to the BCC phase, showing the stability of the BCC structure. In addition to the stability study at 0 K, the atom trajectories from vibration were also examined at 300 K, 600 K and 900 K (see Fig. 3(c)). If there is a tendency of phase transformation, the atom positions will exhibit a large deviation from the ideal BCC lattice sites and show a consistent shift along a specific direction for all atoms, as evidenced in the case of TiZrHf [68]. For NbZrTi, most of the atoms vibrate around BCC lattice sites with a circular distribution profile within the projection plane. Only few atoms (~3 out of 128 atoms) show a deviation from the ideal lattice site at 300 K, and this localized instability
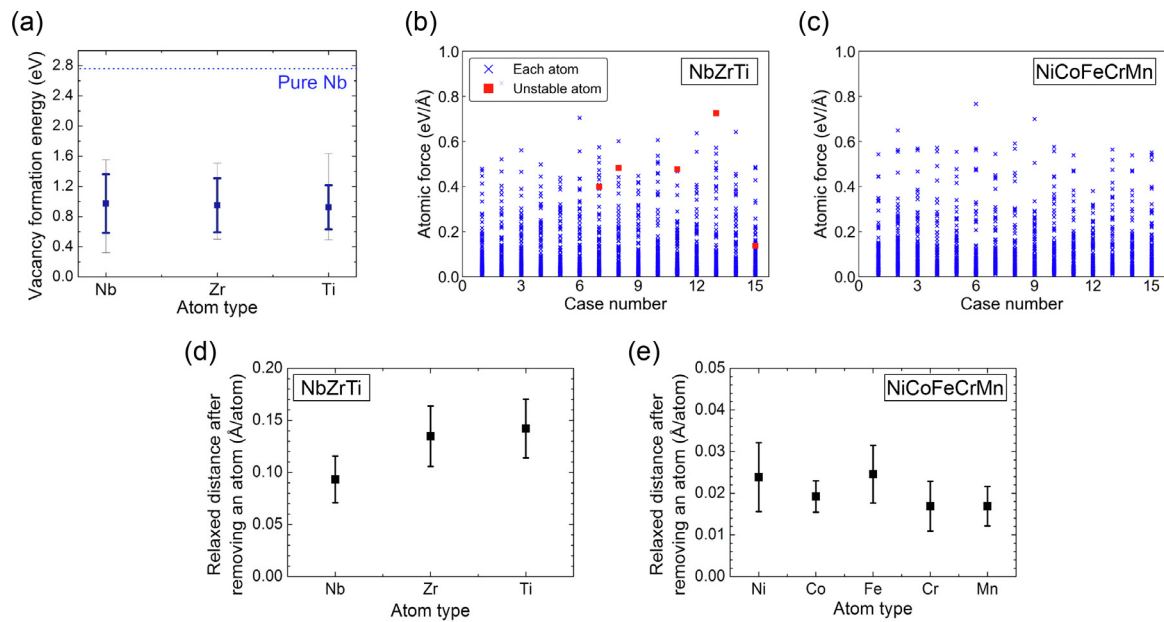
**Fig. 4.** (a) Vacancy formation energy of different types of atoms in NbZrTi (blue error bar: standard deviation; gray error bar: maximum and minimum). (b) Atomic force of each atom in NbZrTi in the unrelaxed structure of Zr vacancy, where the unstable atom refers to the neighbouring atom that fills into the vacancy site during the structural relaxation. In total, 15 Zr vacancy structures were simulated. Results for Nb and Ti vacancies are also included in Fig. S7 of the Supplementary Materials. (c) Atomic force of each atom in NiCoFeCrMn in the unrelaxed vacancy structure. (d-e) Average displacement per atom in NbZrTi and NiCoFeCrMn after removal of a vacancy. (For interpretation of the references to colour in this figure legend, the reader is referred to the web version of this article.)

is greatly reduced at 600 K and 900 K. Based on these analyses, we show that the constructed SQS structure is stable with little dynamical instability.

Based on the parameter of $\Delta d$, the extent of local lattice distortion in NbZrTi is larger than BCC NbTiV and VTaCrW, and similar to AlNbTiV and HEAs from the HfNbTaTiZr-based alloy system [23,61]. Although point defect properties depend on the physical and electronic properties of the constituent elements, the local lattice distortion has a great impact on the structural stability and energy landscape, which also influences the point defect behaviours.

### 3.2. Vacancy

Based on first-principles calculations, the vacancy formation energies ($E_f^v$) of Nb, Zr and Ti are 0.97 eV $\pm$ 0.39 eV, 0.95 eV $\pm$ 0.36 eV and 0.92 eV $\pm$ 0.29 eV, respectively, as shown in Fig. 4(a). There is a wide range of energies for each element and the average energy is approximately equal. The vacancy formation energy is much smaller than those of its constituent elements (2.77 eV from BCC Nb, and 2.00 eV and 2.01 eV from Zr and Ti of HCP structure).

Interestingly, in 24% of the relaxed vacancy structures, the initial vacancy site was filled by a neighbouring atom after energy minimization. For one instance, the new vacancy site was subsequently filled by its own neighbouring atom again. To our best knowledge, this type of instability of vacancy site was not reported in other MEAs or HEAs. There is no clear difference in the local chemical environment around these unstable vacancy sites when the number of each element in the 1NN and 2NN shell is assessed. In addition, these sites are distributed randomly in the studied structure with no clear spatial aggregation. For comparison, vacancy relaxation was also performed in FCC HEA NiCoFeCrMn and no such instability was identified. By comparing the atomic force of each atom in the unrelaxed vacancy structures (see Fig. 4(b) and (c)), it is found that the atomic forces have similar distributions and magnitudes between NbZrTi and NiCoFeCrMn. One might expect that the extreme values of the atomic force in the unrelaxed

structure, corresponding to the neighbouring atoms of the vacancy site, is higher in NbZrTi due to the larger lattice distortion. However, it is shown here that the difference in the initial atomic force is not significant between NbZrTi and NiCoFeCrMn, although two different structures are compared. In addition, the unstable atom that fills into the vacancy site does not necessarily experience a large initial atomic force, which could be quite low in some cases (see Fig. 4(b)). The spontaneous replacement can occur when the path to the vacancy site has no energy barrier regardless of the magnitude of the atomic force. Therefore, it is the unusual local potential landscape that leads to the spontaneous replacement of the vacancy site by the neighbouring atoms. The large lattice distortion changed the potential energy landscape significantly from a lattice-based fluctuation, completely suppressing vacancy migration barriers between certain neighbouring sites, while the slope of the potential of these unusual local sites were not greatly enhanced.

By comparing the atomic displacement during the vacancy relaxation using Eq. (6), it is shown from Fig. 4(d) and (e) that NbZrTi experienced much larger structural adjustment. The average atomic displacement is ∼6 × larger than that of NiCoFeCrMn. The overall larger degree of structural adjustment may lead to the lower $E_f^v$ of NbZrTi compared to that of its constituent elements. One clear evidence is that for unstable vacancy structures with spontaneous exchange with a neighbouring atom, the average $E_f^v$ is 0.69 eV $\pm$ 0.29 eV, which is lower than the overall average $E_f^v$ of 0.95 eV $\pm$ 0.34 eV. The removal of an atom can trigger a large extent of system relaxation, which lowers the total system energy and $E_f^v$. However, there is no strong correlation between individual $E_f^v$ and the total relaxed distance of the system because the contribution of atomic displacement to the lowering of the system energy also depends on the atom locations relative to the vacancy site. The relationships between $E_f^v$ and the number of each element in the 1NN shell, the number of each element in the 1NN and 2NN shell, Bader volume of the removed atom and Bader charge of the removed atom all show weak correlations (see Fig. S8 - Fig. S10 of the Supplementary Materials for the dependence of $E_f^v$ on these

parameters). Further exploration is needed to determine whether a single parameter or combined parameters can be used to estimate the individual vacancy formation energy. Here, we show that due to the large local lattice distortion and local chemical complexity, the structural relaxation is a complicated process and depends heavily on its local environment.

In previous studies of MPEAs, no significant decrease of $E_f^v$ was observed. The average $E_f^v$ of NiFeMnCr HEA is 1.96 eV [21], which is comparable to its constituent elements of Ni [69,70], Fe [69,71], Cr [69] and Mn [71]. In the Ni-containing MPEAs, the average $E_f^v$ is equal or slightly higher than pure Ni [20]. In BCC equiatomic VTaCrW, the $E_f^v$ also has a large energy spread, and the average $E_f^v$ is slightly lower than pure W, but higher than pure Ta [23]. Thus, there seems no clear trend on the relative magnitude of vacancy formation energy compared to pure elements based on previous studies, and such low $E_f^v$ was not observed.

First, lower vacancy formation energy in NbZrTi leads to a higher equilibrium vacancy concentration [55]:

$$C_v = \exp\left(\frac{S_f^v}{k}\right)\exp\left(\frac{-E_f^v}{kT}\right), \tag{7}$$

where $S_f^v$ and $E_f^v$ are vacancy formation entropy and energy, respectively. For example, for a temperature of 1000 K, the $\exp(-E_f^v/kT)$ term is $\sim 10^9$ higher than that of pure Nb. Here, energy calculations were performed at 0 K and we assume that $S_f^v$ does not decrease significantly relative to its constituent elements [72]. Further evaluation of $S_f^v$ is necessary by taking into account different entropy components [73–76]. Recent studies have shown that for a perfect lattice, the change of vibration entropy is of the same magnitude as that of configurational entropy among different BCC MPEAs [43], and entropy can be important in predicting phase stability of binary random solid solutions [77]. From

the perspective of $C_v$, the equivalent average $E_f^v$ should be actually lower than the arithmetic mean due to the wide distribution of $E_f^v$ and the tendency of vacancies to form near low-energy neighborhoods [73]. In addition to the impact on $C_v$, lower vacancy formation energy also indicates that less energy is required to produce a vacancy, which means that vacancy defects can be more easily formed.

These two differences have implications for materials used for nuclear applications. First, radiation-induced swelling is a major concern for long-term mechanical integrity of structural materials. High equilibrium vacancy concentration promotes the thermal emission of vacancies by void, reducing the extent of swelling at high temperature [55]. Second, it is believed that during the initial stage of irradiation when the displacement cascade takes place, the reduced heat dissipation from MPEAs can result in enhanced defect recombination, leading to a lower number of surviving defects after the thermal spike period [26,29,78]. If the defect formation energies are much lower, the same imparted energy from the incident radiation can create a higher number of defects during the thermal spike period, which competes with the aforementioned mechanism of enhanced defect recombination.

Fig. 5(a) shows the distributions of vacancy migration energies ($E_m^v$) in NbZrTi. All three elements have similar wide energy distributions with the lower end extending to nearly 0 eV. This is consistent with previous calculations of vacancy formation energy with no migration barrier. There is a weak correlation between the forward and backward migration energy, showing a Pearson's correlation coefficient of 0.22 (see Fig. 5(b)). We need to emphasize that there is a distinct difference from FCC MPEAs, which usually have stronger positive linear correlations between the forward and backward migration barriers [21,23].
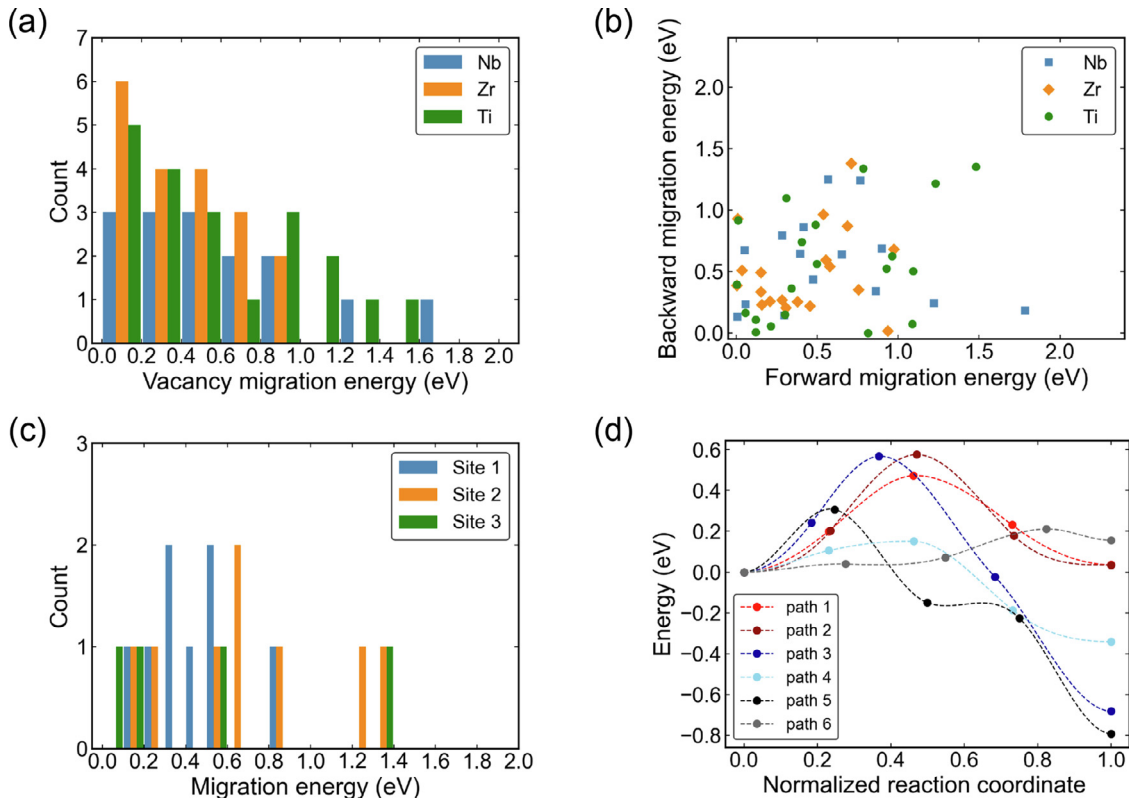


**Fig. 5.** (a) Distribution of vacancy migration energies in NbZrTi. (b) Correlation between the forward and backward migration energy. (c) Vacancy migration energies for paths to all the 1NN sites for three different Nb vacancy sites. (d) Representative vacancy migration barriers. The corresponding transition structures can be found in Fig. S11 of the Supplementary Materials.

Fig. 5(c) lists the migration barriers to all eight neighbouring sites at three different Nb vacancy sites. At the same vacancy site, depending on the migration direction, the energy barrier varies substantially. For instance, the barrier can be 1.4 eV in one direction and 0.1 eV in a different direction. At site 3, several migration paths were unstable, where the final states were spontaneously relaxed to the initial state. Representative migration paths were presented in Fig. 5(d): the path 1 and 2 are conventional barrier profiles with good symmetry; the path 3 and 4 have large differences between forward and backward migration energies; the path 5 and 6 exhibit irregular barrier shapes. All these results indicate that due to the large lattice distortion, the energy landscape could differ significantly at a very local scale. The site-to-site variation is more prominent compared to FCC MPEAs and even some BCC MPEAs [23]. For future material modeling at a larger scale, such as MD and kinetic Monte Carlo (KMC) simulations, these characteristics need to be taken into account to reflect the distinct defect behaviours of NbZrTi.

Due to the wide distribution of the vacancy migration energy, using the arithmetic mean to represent the average migration energy could potentially bias the actual migration behaviours. For each vacancy site, assuming only the vacancy jumps through the 1NN, there are eight possible migration pathways. Since the jump frequency scales with $\exp(-E_m^v/kT)$, the vacancy will preferentially migrate through sites of low $E_m^v$. A simple KMC algorithm was used to estimate the equivalent $E_m^v$. For each migration event, the number of each type of atom in the 1NN shell was randomly generated and $E_m^v$ of the corresponding atom type was randomly assigned to these sites based on the first-principles results. This is supported by the weak correlation among vacancy migration energies at the same site (see Fig. 5(c)). The migration event and step time were then determined based on the Monte Carlo method [79]. Because the correlation between the forward and backward $E_m^v$ is weak (see Fig. 5(b)), we assume that each jump is independent from its previous jump. In total, $10^6$ jumps were computed. Here, we assume that the Debye frequency and vacancy migration entropy do not vary, and we only focus on the impact of the variation of $E_m^v$. The KMC-equivalent mean was then determined by equating the total time and total number of jumps of each element.

As shown in Table 2, the arithmetic mean overestimates the average $E_m^v$ of NbZrTi. This is expected because it is highly likely that the migration takes place quickly through the low $E_m^v$ sites among all eight neighbouring sites. Since the method of arithmetic mean gives equal weight to large $E_m^v$ values, it could give inaccurate $E_m^v$ order among different elements, which affects the analysis related to elemental diffusion and segregation. The KMC method is less sensitive to extreme values from the limited data set, as each jump event is determined collectively from eight different $E_m^v$ values. Based on the KMC method, the average $E_m^v$ is approximately ∼ 0.35 eV, which is smaller than 0.45 eV from pure Nb. For pure Zr, the $E_m^v$ values are 0.54 eV and 0.63 eV for the basal and non-basal migration, respectively [80]. For pure Ti, the basal and non-basal $E_m^v$ energies are 0.40 eV and 0.53 eV [81]. Although Zr and Ti have a different crystal structure, we show here that the $E_m^v$ of NbZrTi is smaller than all of its constituent elements under ambient conditions. We note that in NbZrTi, there is a small difference in $E_m^v$ among Nb, Zr and Ti. Due to the large energy spread of $E_m^v$, more

**Table 3**
Preferred directions for different types of dumbbell interstitials.

| Dumbbell type | Preferred direction | Occurrence probability | Second-preferred direction | Occurrence probability |
|---|---|---|---|---|
| Nb-Ti | <110> | 9/17 | <111> | 7/17 |
| Ti-Ti | <110> | 13/14 | <100> | 1/14 |
| Zr-Ti | <110> | 9/12 | <113> | 2/12 |
| Nb-Nb | <111> | 5/6 | <012> | 1/6 |
| Zr-Nb | <111> | 1/2 | <110> | 1/2 |
| Zr-Zr | <013> | 1/1 | | |

statistics are needed to fully characterize the relative order of $E_m^v$ among different elements.

### 3.3. Interstitial

Different initial structures including <111> dumbbells, <110> dumbbells, <100> dumbbells and tetrahedral sites were simulated, as described in Section 2.1. Among all the configurations, 61% of the interstitials moved to a different lattice site by rotating their directions and replacing other neighbouring atoms. The interstitial instability originates from the irregular energy landscape induced by the large lattice distortion. In the work of Zhao [23], unstable interstitial configurations have also been observed in VTaCrW but were not counted in the calculation of $E_f^i$ due to the involvement of antisite exchange. In this work, those configurations were included in the calculation of $E_f^i$ using Eq. (1). We have them considered because of two factors: (1) they are representative events in NbZrTi, and (2) they have stable final states based on energy minimization.

As shown in Fig. 6(a), in the final configurations, Ti-Ti dumbbell has the lowest formation energy, followed by Ti-Nb and Ti-Zr. Other types are not listed individually due to their limited number of occurrences. The average $E_f^i$ is 1.92 eV ± 0.39 eV, much lower than 4.38 eV of the most stable <111> dumbbell of pure Nb. For pure Zr and Ti with HCP structure under ambient conditions, according to different studies, the $E_f^i$ values for the most stable interstitial configuration are in the range of 2.70 eV – 3.03 eV and 2.27 eV – 2.42 eV, respectively, which are also larger than that of NbZrTi [39,40,80,82]. The occurrence probabilities of interstitial configurations with low $E_f^i$ have a higher tendency to form (see Fig. 6(b) and (c)). The occurrence probability here corresponds to static calculations with the same number of each type of atom being added in the initial structures. For dynamic simulations, such as cascade collision simulations for radiation damage studies, we still expect a higher occurrence probability of Ti-containing interstitials and a lower probability of Zr-containing interstitials based on $E_f^i$. However, we note that the defect formation dynamics is not reflected from static calculations.

The preferred dumbbell directions are different for different types of atoms, as presented in Table 3. For example, the Nb-Ti interstitial can form both <110> and <111> dumbbells, but Ti-Ti and Nb-Nb pair have a strong preference for <110> dumbbell and <111> dumbbell, respectively. Due to the large distortion of the lattice, unusual dumbbell directions can be formed. For the same initial interstitial site with different dumbbell directions, the final configurations can be different, as illustrated in Table 4. The location of the final interstitial site can be far away from the initial

**Table 2**
Average vacancy migration energy based on the KMC-equivalent method and the arithmetic mean. The jump percentage of each type of atom is normalized by the total number of jumps from the KMC method.

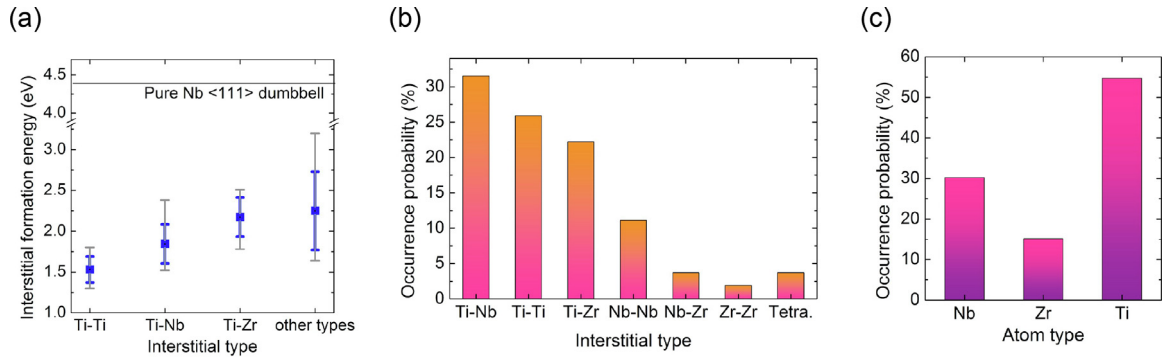| Atom type | KMC-equivalent mean at 1000 K (eV) | Jump percentage (%) | Arithmetic mean (eV) | Jump percentage (%) |
|---|---|---|---|---|
| Nb | 0.352 | 33.3 | 0.526 ± 0.506 | 4.8 |
| Zr | 0.348 | 34.5 | 0.378 ± 0.298 | 20.0 |
| Ti | 0.354 | 32.2 | 0.498 ± 0.388 | 6.5 |

**Fig. 6.** (a) Interstitial formation energies for different final interstitial configurations (blue error bar: standard deviation; gray error bar: maximum and minimum). (b) Occurrence probabilities of different types of final interstitial configurations. (c) Occurrence probabilities of different elements in the final interstitial configurations. (For interpretation of the references to colour in this figure legend, the reader is referred to the web version of this article.)
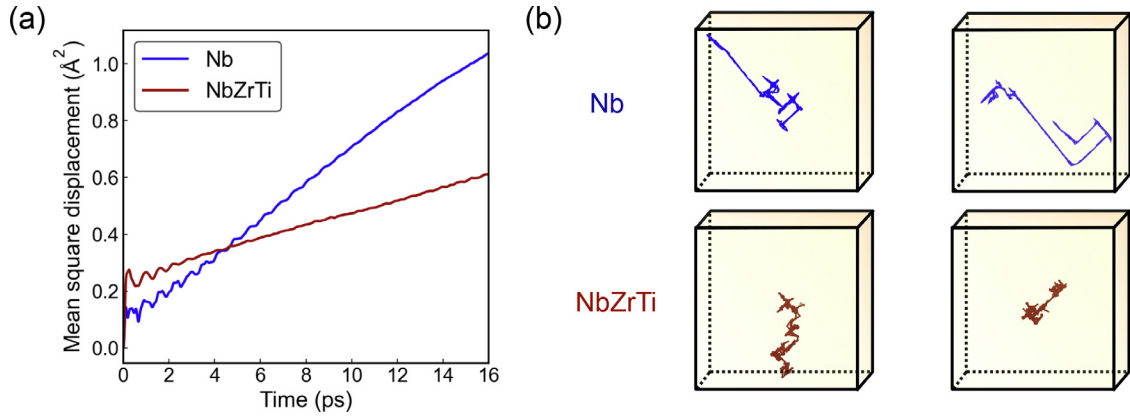


**Fig. 7.** (a) Mean square displacement of interstitial migration in NbZrTi and Nb at 1200 K. (b) Representative trajectories of interstitial pairs in NbZrTi and Nb with the same diffusion time scale. The interstitial trajectories are unwrapped from the simulation box with periodic boundaries and are enclosed here in boxes of the same length scale.

**Table 4**

Stable final interstitial configurations at the same initial lattice site with different initial orientations for a Nb-Nb dumbbell. The corresponding final structures are provided in Fig. S12 of the Supplementary Materials ($L_c$: lattice parameter, $D_{initial-final}$: distance between the initial and final interstitial site).

| Initial dumbbell direction | Final dumbbell configuration | $D_{initial-final}$ | $E_f^i$ (eV) |
|---|---|---|---|
| [111], [110], [101], [011] | Ti-Ti [010] | $\sqrt{3}L_c$ | 1.82 |
| [1$\bar{1}$1], [01$\bar{1}$] | Ti-Ti [011] | $\sqrt{3}L_c$ | 1.79 |
| [1$\bar{1}\bar{1}$], [1$\bar{1}$0], [10$\bar{1}$] | Ti-Ti [011] | $2\sqrt{3}L_c$ | 1.31 |
| [11$\bar{1}$] | Nb-Ti [11$\bar{1}$] | $1.5\sqrt{3}L_c$ | 1.61 |

site and the $E_f^i$ of the stable interstitials can also be different. For nuclear materials, the interstitial structures and formation energies have a great impact on the dislocation loop nucleation, which further impacts the irradiation hardening and defect microstructure evolution [55,83–86].

The interstitial migration behaviours were studied by AIMD simulations at a temperature of 1200 K. NbZrTi has a lower MSD than pure Nb due to the more tortuous migration pathways (see Fig. 7). The diffusion coefficients for Nb and NbZrTi are $1.02 \times 10^{-10}$ m$^2$/s and $3.88 \times 10^{-11}$ m$^2$/s, respectively, according to the Einstein relation [87]. The interstitial atom in pure Nb can form long one-dimensional (1D) diffusion path along <111> direction, whereas the interstitial atom in NbZrTi diffuses in a three-dimensional (3D) manner with more frequent changes of directions. The 3D migration behaviour leads to a larger cross section of interactions with defects of low mobility, such as vacancy and vacancy clusters, and enhances the defect recombination [88]. The jump rate for NbZrTi is actually 9.6% higher than that of Nb, but

due to the 3D spatial migration behaviour, the diffusion coefficient is only 38% of Nb at 1200 K.

The correlation factor $f_c$ is used to examine the angular correlation between consecutive jumps [19,88]:

$$f_c = \frac{1 + \overline{\cos\theta}}{1 - \overline{\cos\theta}}, \quad (8)$$

where $\theta$ is the angle between two consecutive jumps and $f_c$ is calculated by averaging $\cos\theta$ over all trajectories. Nb and NbZrTi have a $f_c$ of 0.19 and 0.20, respectively, showing negligible difference. A value between 0 and 1 means that there is a tendency for the next jump to return back to the initial location of the previous jump. Although the average angular correlation between consecutive jumps is similar, two mechanisms contribute to the difference in diffusion coefficients between Nb and NbZrTi. First, interstitial atoms in NbZrTi have their own preferred dumbbell directions and have a higher probability to rotate their orientations (see Table 3). Therefore, it is more difficult to maintain the same 1D <111> direction. Second, certain lattice sites can act as "trap sites" for interstitial atoms and make it difficult for interstitials to escape their surroundings. Based on the AIMD trajectories, there are six lattice sites in NbZrTi that an interstitial spends longer time at or returns to for more number of times compared to the maximum case from pure Nb. In addition to the stability of these sites, we also conjecture that as a large fraction of interstitial structures are unstable at their initial sites, the distance between stable interstitial structures is farther than the regular atomic spacing from conventional materials. Once an interstitial is trapped at a stable site, it is more difficult to escape due to the longer distance from the neighbouring stable site. However, this needs further confirmation by simulations at a larger scale.
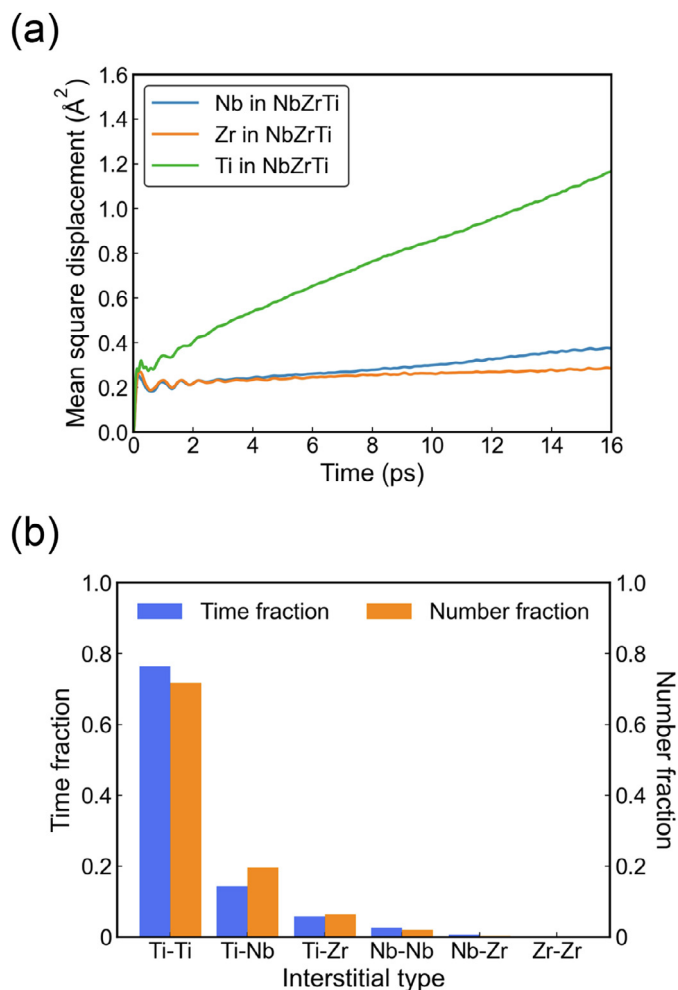
## (a)



## (b)



**Fig. 8.** (a) Mean square displacement of different elements in NbZrTi at 1200 K. (b) Time fraction and number fraction of interstitial sites of different dumbbell types.

In NbZrTi, Ti diffuses much faster than Nb and Zr, as shown in Fig. 8. By examining the time fraction and number fraction of each type of interstitial, we find that Ti-Ti dumbbell has the highest occurrence probability, followed by Ti-Nb and Ti-Zr. In contrast, Nb-Zr and Zr-Zr dumbbells have the lowest probability to form. This is in good agreement with the order of $E_f^i$ (see Fig. 6), where Ti-Ti dumbbell has the lowest $E_f^i$ and Zr-containing interstitials tend to have higher $E_f^i$. For each type of interstitials, the time fraction and number fraction have similar values because different interstitial pairs have similar distributions of dwelling time at each site (see Fig. S13 of the Supplementary Materials for the dwelling time distribution of different interstitial pairs). According to the model for radiation-induced segregation [89], assuming the vacancy diffusion behaviours are identical for different alloy elements, a strong binding of interstitials to a certain type of atom leads to a higher tendency of its segregation near defect sinks, such as surface or grain boundary [55]. Here, Ti atom is preferentially associated with the interstitial, which can be explained by its positive binding energy, i.e., the energy of converting one type of interstitial to the preferred type of interstitial [55]. Thus, Ti atom diffuses faster through the interstitial diffusion mechanism. The overall segregation behaviour is then determined collectively by the interstitial and vacancy diffusion mechanism [90–92].

Attempts have been made to tune the interstitial diffusion behaviours through changing the elemental composition and local atomic bonding. The first attempt is to reduce Ti composition to reduce the diffusion of Ti. When the composition changes from equiatomic NbZrTi to $Nb_{0.4}Zr_{0.4}Ti_{0.2}$, as shown in Fig. 9(a) and (b), the total diffusion coefficient is reduced due to the decrease of Ti content and the corresponding decrease of Nb and Ti diffusion coefficients. The Ti-Ti dumbbell becomes less easily formed due to the reduced Ti composition. Accordingly, the proportions of Ti-Nb and Ti-Zr dumbbells become higher (see Fig. 9(c)). As the preferential Ti diffusion is promoted by the preferential interstitial binding of Ti-Ti pair, Ti diffusion coefficient becomes lower. Although the fraction of Ti-Nb dumbbell becomes higher, the Ti atom in Ti-Nb dumbbell is more active and the Nb atom is relatively immobile, which leads to the lower Nb diffusion coefficient.

The second attempt is to study the impact of SRO structure while keeping the same equiatomic composition. The SRO structure was created by a combined Metropolis MC and density functional theory (DFT) scheme, as described in Section 2.1. The overall diffusion coefficient is reduced due to the decrease of Ti and Nb diffusion coefficients (see Fig. 9(d) and (e)). Fig. 1(b) shows that the SRO structure has a strong tendency of Nb-Nb clustering and a moderate tendency of Zr-Ti clustering. Interestingly, the interstitial prefers to migrate in the Ti- and Zr-enriched region as revealed by the diffusion trajectories, which leads to the lower diffusion coefficient of Nb. This can also be reflected by the decrease of Ti-Nb dumbbell fraction and the increase of Ti-Zr dumbbell fraction (see Fig. 9(f)). As the interstitial is mostly confined in the Ti- and Zr-enriched region, the long-range diffusion becomes less favoured, which results in the decrease of elemental and total diffusion coefficients. The ordering tendencies among different atom pairs all have an impact on the interstitial migration behaviour. In contrast to these two structural tuning methods, another attempt by simply reducing the percentage of the fast diffusion species of Ti atom in the 1NN shell shows no improvement for the reduction of Ti and total diffusion coefficients (see Section 2 of Supplementary Materials for the comparison).

### 3.4. Ion irradiation experiment

To study the impact of point defect energy on radiation-induced void swelling, ion irradiation experiment was performed at 675 °C with 3-MeV Fe ions at a fluence of $1.02 \times 10^{17}$ ions/cm$^2$, corresponding to a peak dose of 99.8 dpa and 129 dpa in Nb and NbZrTi, respectively. Void swelling is known to be pronounced at intermediate homologous temperature (T/T$_m$) because the void growth is limited by the low defect mobility at low temperature and is limited by the high vacancy supersaturation concentration at high temperature [55]. As explained in Section 3.2, the vacancy formation energy of NbZrTi is much lower than that of pure Nb, the equilibrium vacancy concentration should be significantly higher, limiting the void formation at high temperature. According to previous experiments [93–97], voids can be formed in Nb by heavy ion irradiation from 650 °C to 1120 °C, corresponding to a T/T$_m$ of 0.34 to 0.51. With 3.3-MeV $^{58}$Ni$^+$ ions, the maximum void swelling occurred at a temperature of 1010 °C, corresponding to a T/T$_m$ of 0.47 [93]. Based on these previous efforts, an irradiation temperature of 675 °C was selected because in addition to the expected void formation in Nb at this temperature, a T/T$_m$ of 0.48 in NbZrTi [98] is also in the normal void swelling temperature window [55]. Furthermore, this temperature falls into the operating temperature range of fourth-generation nuclear reactors including gas-cooled fast reactor and molten salt reactor [8,9].

As shown in Fig. 10(a), in the irradiated region of pure Nb, voids and dislocation loops were formed by agglomeration of vacancies and interstitial atoms. Dislocation loops were also formed outside the SRIM-predicted ion range by diffusion of radiation-induced defects at high temperature. A great number of voids were observed
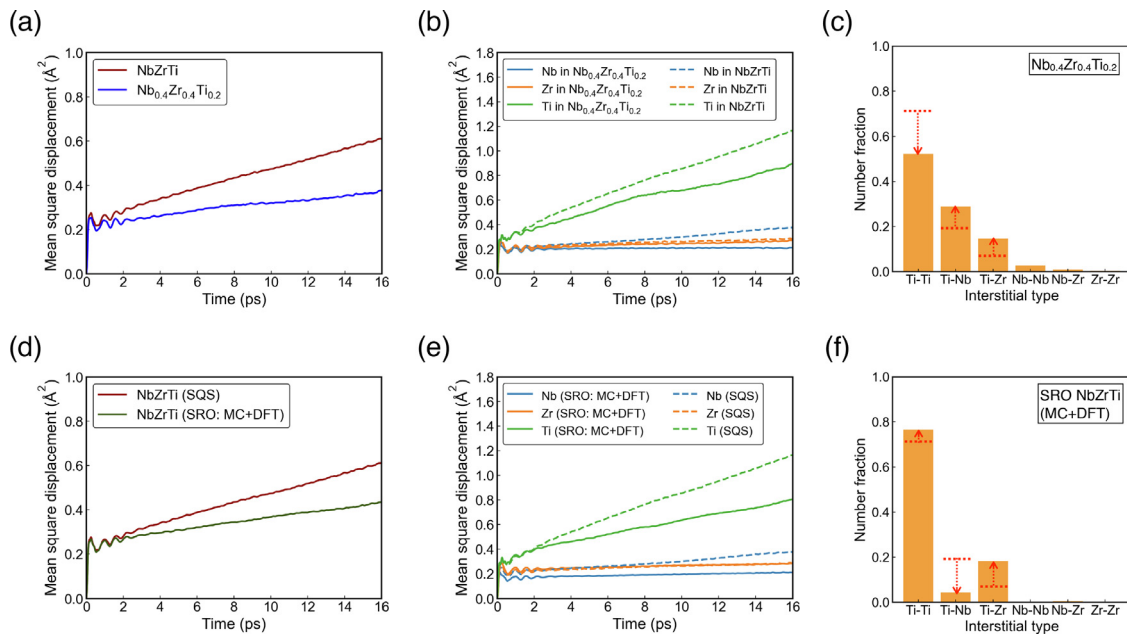
**Fig. 9.** (a-b) Comparison of MSD of interstitial migration between NbZrTi and $Nb_{0.4}Zr_{0.4}Ti_{0.2}$. (c) Number fraction of different dumbbell types in $Nb_{0.4}Zr_{0.4}Ti_{0.2}$. (d-e) Comparison of MSD between SQS-based NbZrTi and NbZrTi with a SRO structure based on the MC + DFT method. (f) Number fraction of different dumbbell types in NbZrTi with a SRO structure based on the MC + DFT method. The dotted lines in (c) and (f) represent the results from the SQS-based NbZrTi structure.
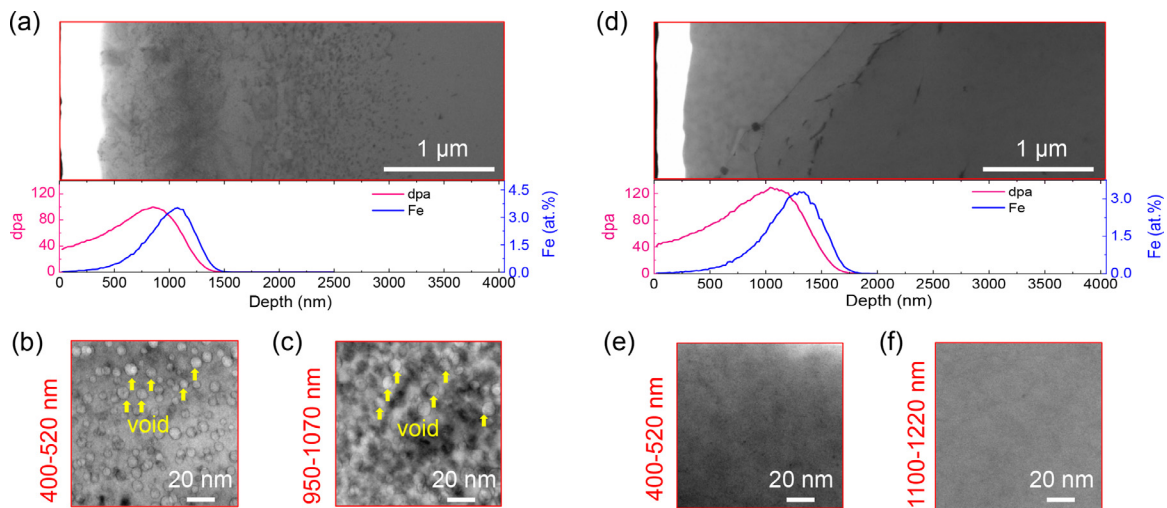


**Fig. 10.** (a) Cross-sectional STEM-BF image of Nb irradiated at 675 °C. Depth profiles of the dpa and Fe ion concentration predicted by the SRIM code are shown. (b-c) BF TEM images of void formation in the irradiated regions of pure Nb at two different depths acquired at under-focused condition. (d) Cross-sectional STEM-BF image of NbZrTi irradiated at 675 °C along with the depth profiles of dpa and Fe ion concentration. (e-f) No formation of voids and visible defect microstructures in the irradiated NbZrTi.

throughout the irradiation area with an average diameter of 5.5 nm ± 1.7 nm (see Fig. 10(b) and (c)). In contrast, no voids and other radiation-induced defect microstructures were observed in NbZrTi, as shown in Fig. 10(d) – (f). The dislocation lines at a depth range of 1500 nm – 2500 nm correspond to pre-irradiation defects. The energy dispersive spectroscopy (EDS) mapping also showed that the spatial distributions of Nb, Zr and Ti are uniform in the irradiated and unirradiated region, and the atomic composition remains equiatomic (see Fig. S14 and Table S4 of the Supplementary materials for the EDS mapping results). As expected, the higher equilibrium vacancy concentration limits the growth of voids, where the vacancy influx to voids are counterbalanced by the thermal vacancy emission [55].

In addition, the enhanced recombination of point defects contribute to the observation of reduced defects. As reported for FCC Ni-based MPEAs and BCC VTaCrW [20,23], the recombination probability of point defects should be higher than pure metals due to the closer mobility between the vacancy and interstitial atom. When the point defect recombination is higher, there are less surviving defects that can further agglomerate into large defect microstructures, such as voids and dislocation loops. This has been considered as one of the important mechanisms for the enhanced radiation resistance of HEAs [20,26]. The same mechanism applies to NbZrTi because of the lower average vacancy migration energy (see Table 2) and lower interstitial diffusion coefficient (see Fig. 7), i.e, higher vacancy mobility and lower interstitial mobility. However, with lower vacancy and interstitial formation energy, more vacancies and interstitial atoms are created during the thermal spike period. The relevant importance of these two competing mechanisms needs to be further evaluated.

## 4. Discussions

Based on first-principles calculations, NbZrTi exhibits distinctive point defect properties from pure Nb. The average vacancy formation energy is 0.95 eV $\pm$ 0.34 eV compared to 2.77 eV in Nb. The average interstitial formation energy is 1.92 eV $\pm$ 0.34 eV, whereas the interstitial formation energies in Nb are 4.38 eV – 5.12 eV for different interstitial configurations. In NbZrTi, the interstitial formation energy has a strong dependence on the dumbbell atom types, which can be clearly seen from Fig. 6(a). The dependence on the dumbbell orientation is insignificant relative to the site-to-site variation. For example, for a final configuration of <110> dumbbell and <111> dumbbell, the average energies are 1.83 $\pm$ 0.37 eV and 2.07 $\pm$ 0.49 eV, respectively. The difference could also be attributed to the preferential formation of <110> dumbbell of the most stable Ti-Ti pair. According to the KMC-equivalent method computed at 1000 K (see Table 2), the average vacancy migration energy is ~0.35 eV in NbZrTi, which is lower than 0.45 eV from pure Nb. Based on AIMD simulations, the interstitial diffusion coefficient in NbZrTi is 38% of that in Nb at 1200 K. In summary, NbZrTi has much lower vacancy and interstitial formation energies, higher vacancy mobility and lower interstitial mobility.

The instability of defect structures was observed in both vacancy and interstitial configurations. In the vacancy structures, it was manifested by the spontaneous replacement of the vacancy site by a neighbouring atom, whereas in the interstitial structures, it was manifested by the large relaxation distance of the interstitial atom away from the initial interstitial site (see Table 4). This can be attributed to the severe lattice distortion of NbZrTi that leads to an irregular energy landscape (see Fig. 5(d)) and the resulting suppression of migration barriers at local sites. The lower vacancy formation and interstitial formation energies can also be explained by the large degree of relaxation resulting from such an irregular energy landscape. The BCC VTaCrW, which has only interstitial instability, has a local lattice distortion parameter $\Delta d$ of 0.087 Å [23], which is smaller than 0.171 Å from NbZrTi. It is also reported that BCC MEA VTaTi and VTaW have lower interstitial formation energies due to the large local relaxation based on classical molecular static simulations [33]. For comparison, the $\Delta d$ values of VTaTi and VTaW were calculated by first-principles calculations and were found to be 0.132 Å and 0.061 Å, respectively, which are also smaller than that of NbZrTi. By comparing different BCC MPEAs, there seems to be a trend that with the increase of lattice distortion, the structural instability extends from interstitial structures to vacancy structures and leads to the decrease of the corresponding defect formation energy. NbZrTi-based MPEAs, such as NbZrTiTaHf and NbZrTiHf, all have similar or even larger $\Delta d$ values, ranging from 0.16 Å– 0.20 Å [61]. Thus, it is worth exploring further whether these alloys have similar low point defect formation energies and large extent of defect structural relaxation.

As explained previously, it was proposed that the point defect recombination in MPEAs is higher than pure elements under irradiation due to the closer mobility between vacancies and interstitials [20]. This was largely attributed to the slower diffusion of interstitial atoms and the overlap between vacancy and interstitial migration energy distributions. Here, due to the extremely large distribution of vacancy migration energy and also the skewed distribution profile towards low energy (see Fig. 5(a)), the vacancy migration can occur much more easily because the probability of migration through a low migration barrier is high. Therefore, the higher vacancy mobility can further enhance the point defect recombination under irradiation. It is noted that higher mobility of vacancy can also promote the clustering of vacancies by increasing the vacancy arrival rate at void embryos [55]. Considering also the other distinct point defect properties, the overall impact on irradiation resistance could differ significantly from FCC MPEAs and needs to be further evaluated with MD simulations and irradiation experiments.

Regarding the diffusion capabilities of different elements, Nb, Zr and Ti have similar vacancy migration energies (see Table 2), and the relative energy difference cannot be clearly distinguished. On the other hand, interstitial diffusion through Ti is much faster than Zr and Ti (see Fig. 8) due to the preferential binding of interstitials with Ti atom. The reduction of Ti content in NbZrTi and the creation of low-energy SRO structure based on the lattice MC method are both effective in decreasing the Ti and total diffusion coefficients. A slower diffusion coefficient is usually associated with more trapping around certain lattice sites or within certain local regions, leading to a lower probability of long-range diffusion. When there is a strong short-range clustering tendency of atom pairs in NbZrTi, the diffusion of interstitials is preferred in regions where Zr and Ti are enriched, which limits the long-range interstitial diffusion. The existence of SRO structure has been confirmed experimentally and has shown great impact on the mechanical and radiation properties of MPEAs [99–101]. In this work, a SQS model with no SRO was used to calculate the defect properties, but the actual local ordering tendency in BCC MPEAs could complicate the defect properties, which needs additional investigation [102].

The obtained first-principles results are useful for the validation of interatomic potentials. A systematic comparison of point defect properties of NbZrTi, including vacancy formation energy, vacancy migration energy and interstitial formation energy, was demonstrated with an EAM potential with potential parameters taken from Ref. [103,104] (see Section 3 of Supplementary Materials for the detailed analysis). Although a quantitative agreement was not fully reached, several conclusions or implications can be drawn from such comparison. First, accurate defect energies from pure metal elements need to be guaranteed. For instance, the underestimation of interstitial formation energy of pure Nb leads to the underestimation of Nb-containing interstitial formation energies in NbZrTi. Second, the EAM potential with a relatively simple formalism is able to capture some important characteristics of NbZrTi, including lower vacancy and interstitial formation energy, unstable initial vacancy and interstitial structures, as well as wide energy distribution in vacancy migration energy. Third, the currently used EAM potential underestimates the lattice distortion and overestimates the defect formation energies. This seems aligned with our conjecture that the decrease of defect formation energies is correlated with the increase of lattice distortion. A good agreement on lattice distortion relies on an accurate description of cross interactions among principal elements.

According to the ion irradiation experiment at 675 °C, we showed that the concept of MPEAs can greatly modify the point defect properties and lead to a different response to the irradiation temperature. Compared to void swelling in Nb at both an absolute temperature of 675 °C and a homologous temperature of 0.48 [93], negligible radiation-induced defects were observed in NbZrTi under the same condition. The reduction in swelling at high temperature is aligned with the high equilibrium vacancy concentration originating from the low vacancy formation energy. The increase of the point defect recombination also plays an important role in the reduction of radiation-induced defects. The characteristics of radiation-induced defects at a range of temperatures and simulations of defect cluster behaviours need to be studied in the future to fully understand the irradiation response of NbZrTi.

## 5. Conclusions

First-principles calculations were performed to assess the vacancy and interstitial formation energies and their migration behaviours in body-centered cubic medium-entropy alloy NbZrTi. Due to the irregular energy landscape induced by the large lo-

cal lattice distortion, unusual structural instability was observed in both vacancy and interstitial structures. Compared to pure Nb, NbZrTi exhibits much lower vacancy and interstitial formation energies, higher vacancy mobility and lower interstitial mobility. Because of the wide energy distribution and the preferential vacancy migration through low-energy sites, the equivalent vacancy migration energy is lower than pure Nb. The slower interstitial diffusion and the chemically-biased diffusion among constituent elements are highly related to the stability of different interstitial configurations. The atomic composition and chemical short-range order can influence the elemental and total interstitial diffusion behaviour. The obtained first-principle results are useful for the benchmark of classical interatomic potential for defect studies. The ion irradiation experiment at 675 °C with 3-MeV Fe ions at a total dose of ~100 dpa showed reduced void swelling in NbZrTi, which is consistent with the high equilibrium vacancy concentration induced by the low vacancy formation energy and enhanced point defect recombination induced by the closer mobility between vacancies and interstitials.

## Declaration of Competing Interest

The authors declare that they have no known competing financial interests or personal relationships that could have appeared to influence the work reported in this paper.

## Acknowledgement

## Supplementary material

Supplementary material associated with this article can be found, in the online version, at doi:10.1016/j.actamat.2022.117806.

## References

[1] M.-H. Tsai, J.-W. Yeh, High-entropy alloys: a critical review, Mater. Res. Lett. 2 (3) (2014) 107–123.

[2] E.P. George, W. Curtin, C.C. Tasan, High entropy alloys: a focused review of mechanical properties and deformation mechanisms, Acta Mater. 188 (2020) 435–474.

[3] O.N. Senkov, D.B. Miracle, K.J. Chaput, J.-P. Couzinie, Development and exploration of refractory high entropy alloys–a review, J. Mater. Res. 33 (19) (2018) 3092–3128.

[4] C. Lu, L. Niu, N. Chen, K. Jin, T. Yang, P. Xiu, Y. Zhang, F. Gao, H. Bei, S. Shi, M.-R. He, I.M. Robertson, W.J. Weber, L. Wang, Enhancing radiation tolerance by controlling defect mobility and migration pathways in multicomponent single-phase alloys, Nat. Commun. 7 (1) (2016) 1–8.

[5] Y.-M. Hu, X.-D. Liu, N.-N. Guo, L. Wang, Y.-Q. Su, J.-J. Guo, Microstructure and mechanical properties of NbZrTi and NbHfZrTi alloys, Rare Metals 38 (9) (2019) 840–847.

[6] X. Duan, Z. Zhang, H. He, Z. Liu, X. Duan, B. Shan, A systematic investigation on quaternary NbTiZr-based refractory high entropy alloys using empirical parameters and first principles calculations, Modell. Simul. Mater. Sci. Eng. (2021).

[7] T. Shi, P.-H. Lei, X. Yan, J. Li, Y.-D. Zhou, Y.-P. Wang, Z.-X. Su, Y.-K. Dou, X.-F. He, D. Yun, et al., Current development of body-centered cubic high-entropy alloys for nuclear applications, Tungsten (2021) 1–21.

[8] P. Yvon, F. Carré, Structural materials challenges for advanced reactor systems, J. Nucl. Mater. 385 (2) (2009) 217–222.

[9] S.J. Zinkle, J.T. Busby, Structural materials for fission & fusion energy, Mater. Today 12 (11) (2009) 12–19.

[10] Y. Wu, Y. Cai, T. Wang, J. Si, J. Zhu, Y. Wang, X. Hui, A refractory $Hf_{25}Nb_{25}Ti_{25}Zr_{25}$ high-entropy alloy with excellent structural stability and tensile properties, Mater. Lett. 130 (2014) 277–280.

[11] O. Senkov, J. Scott, S. Senkova, D. Miracle, C. Woodward, Microstructure and room temperature properties of a high-entropy TaNbHfZrTi alloy, J. Alloys Compd. 509 (20) (2011) 6043–6048.

[12] O. Senkov, J. Scott, S. Senkova, F. Meisenkothen, D. Miracle, C. Woodward, Microstructure and elevated temperature properties of a refractory TaNbHfZrTi alloy, J. Mater. Sci. 47 (9) (2012) 4062–4074.

[13] Y. Wu, Y. Cai, X. Chen, T. Wang, J. Si, L. Wang, Y. Wang, X. Hui, Phase composition and solid solution strengthening effect in TiZrNbMoV high-entropy alloys, Mater. Des. 83 (2015) 651–660.

[14] S. Zhang, Z. Wang, H. Yang, J. Qiao, Z. Wang, Y. Wu, Ultra-high strain-rate strengthening in ductile refractory high entropy alloys upon dynamic loading, Intermetallics 121 (2020) 106699.

[15] Y. Wu, J. Si, D. Lin, T. Wang, W.Y. Wang, Y. Wang, Z. Liu, X. Hui, Phase stability and mechanical properties of AlHfNbTiZr high-entropy alloys, Mater. Sci. Eng. A 724 (2018) 249–259.

[16] B. Singh, J. Evans, Significant differences in defect accumulation behaviour between fcc and bcc crystals under cascade damage conditions, J. Nucl. Mater. 226 (3) (1995) 277–285.

[17] K. Gan, D. Yan, S. Zhu, Z. Li, Interstitial effects on the incipient plasticity and dislocation behavior of a metastable high-entropy alloy: nanoindentation experiments and statistical modeling, Acta Mater. 206 (2021) 116633.

[18] S. Middleburgh, D. King, G. Lumpkin, M. Cortie, L. Edwards, Segregation and migration of species in the CrCoFeNi high entropy alloy, J. Alloys Compd. 599 (2014) 179–182.

[19] S. Zhao, Y. Osetsky, Y. Zhang, Preferential diffusion in concentrated solid solution alloys: NiFe, NiCo and NiCoCr, Acta Mater. 128 (2017) 391–399.

[20] S. Zhao, G.M. Stocks, Y. Zhang, Defect energetics of concentrated solid-solution alloys from *ab initio* calculations: $Ni_{0.5}Co_{0.5}$, $Ni_{0.5}Fe_{0.5}$, $Ni_{0.8}Fe_{0.2}$ and $Ni_{0.8}Cr_{0.2}$, PCCP 18 (34) (2016) 24043–24056.

[21] C. Li, J. Yin, K. Odbadrakh, B.C. Sales, S.J. Zinkle, G.M. Stocks, B.D. Wirth, First principle study of magnetism and vacancy energetics in a near equimolar NiFeMnCr high entropy alloy, J. Appl. Phys. 125 (15) (2019) 155103.

[22] H. Guan, S. Huang, J. Ding, F. Tian, Q. Xu, J. Zhao, Chemical environment and magnetic moment effects on point defect formations in CoCrNi-based concentrated solid-solution alloys, Acta Mater. 187 (2020) 122–134.

[23] S. Zhao, Defect properties in a VTaCrW equiatomic high entropy alloy (HEA) with the body centered cubic (bcc) structure, J. Mater. Sci. Technol. 44 (2020) 133–139.

[24] K. Jin, C. Lu, L. Wang, J. Qu, W. Weber, Y. Zhang, H. Bei, Effects of compositional complexity on the ion-irradiation induced swelling and hardening in Ni-containing equiatomic alloys, Scr. Mater. 119 (2016) 65–70.

[25] C. Lu, T. Yang, K. Jin, N. Gao, P. Xiu, Y. Zhang, F. Gao, H. Bei, W.J. Weber, K. Sun, et al., Radiation-induced segregation on defect clusters in single-phase concentrated solid-solution alloys, Acta Mater. 127 (2017) 98–107.

[26] Y. Zhang, G.M. Stocks, K. Jin, C. Lu, H. Bei, B.C. Sales, L. Wang, L.K. Béland, R.E. Stoller, G.D. Samolyuk, et al., Influence of chemical disorder on energy dissipation and defect evolution in concentrated solid solution alloys, Nat. Commun. 6 (1) (2015) 1–9.

[27] C. Parkin, M. Moorehead, M. Elbakhshwan, J. Hu, W.-Y. Chen, M. Li, L. He, K. Sridharan, A. Couet, In situ microstructural evolution in face-centered and body-centered cubic complex concentrated solid-solution alloys under heavy ion irradiation, Acta Mater. 198 (2020) 85–99.

[28] Q. Peng, F. Meng, Y. Yang, C. Lu, H. Deng, L. Wang, S. De, F. Gao, Shockwave generates <100> dislocation loops in bcc iron, Nat. Commun. 9 (1) (2018) 1–6.

[29] Y. Lin, T. Yang, L. Lang, C. Shan, H. Deng, W. Hu, F. Gao, Enhanced radiation tolerance of the Ni-Co-Cr-Fe high-entropy alloy as revealed from primary damage, Acta Mater. 196 (2020) 133–143.

[30] O. Deluigi, R. Pasianot, F. Valencia, A. Caro, D. Farkas, E. Bringa, Simulations of primary damage in a high entropy alloy: probing enhanced radiation resistance, Acta Mater. 213 (2021) 116951.

[31] J. Byggmästar, K. Nordlund, F. Djurabekova, Modeling refractory high-entropy alloys with efficient machine-learned interatomic potentials: defects and segregation, arXiv preprint arXiv:2106.03369 (2021).

[32] R. Qiu, Y. Chen, X. Liao, X. He, W. Yang, W. Hu, H. Deng, Finnis–Sinclair-type potential for atomistic simulation of defects behaviour in V-Ti-Ta ternary system, J. Nucl. Mater. (2021) 153231.

[33] S. Zhao, Y. Xiong, S. Ma, J. Zhang, B. Xu, J.-J. Kai, Defect accumulation and evolution in refractory multi-principal element alloys, Acta Mater. (2021) 117233.

[34] P.E. Blöchl, Projector augmented-wave method, Phys. Rev. B 50 (24) (1994) 17953.

[35] M. Ernzerhof, G.E. Scuseria, Assessment of the Perdew–Burke–Ernzerhof exchange-correlation functional, J. Chem. Phys. 110 (11) (1999) 5029–5036.

[36] A. Zunger, S.-H. Wei, L. Ferreira, J.E. Bernard, Special quasirandom structures, Phys. Rev. Lett. 65 (3) (1990) 353.

[37] M.C. Gao, C. Niu, C. Jiang, D.L. Irving, Applications of Special Quasi-random Structures to High-entropy Alloys, in: High-Entropy Alloys, Springer, 2016, pp. 333–368.

[38] A. Van De Walle, M. Asta, G. Ceder, The alloy theoretic automated toolkit: a user guide, Calphad 26 (4) (2002) 539–553.

[39] G. Vérité, C. Domain, C.-C. Fu, P. Gasca, A. Legris, F. Willaime, Self-interstitial defects in hexagonal close packed metals revisited: evidence for low-symmetry configurations in ti, zr, and hf, Phys. Rev. B 87 (13) (2013) 134108.

[40] Q. Peng, W. Ji, H. Huang, S. De, Stability of self-interstitial atoms in hcp-Zr, J. Nucl. Mater. 429 (1–3) (2012) 233–236.

[41] D. Nguyen-Manh, A. Horsfield, S. Dudarev, Self-interstitial atom defects in bcc transition metals: group-specific trends, Phys. Rev. B 73 (2) (2006) 020101.

[42] Y. Ikeda, A. Carreras, A. Seko, A. Togo, I. Tanaka, Mode decomposition based on crystallographic symmetry in the band-unfolding method, Phys. Rev. B 95 (2) (2017) 024305.

[43] F. Körmann, Y. Ikeda, B. Grabowski, M.H. Sluiter, Phonon broadening in high entropy alloys, npj Comput. Mater. 3 (1) (2017) 1–9.

[44] A. Togo, I. Tanaka, First principles phonon calculations in materials science, Scr. Mater. 108 (2015) 1–5.

[45] B. Widom, Some topics in the theory of fluids, J. Chem. Phys. 39 (11) (1963) 2808–2812.

[46] W. Tang, E. Sanville, G. Henkelman, A grid-based Bader analysis algorithm without lattice bias, J. Phys. 21 (8) (2009) 084204.

[47] G. Henkelman, B.P. Uberuaga, H. Jónsson, A climbing image nudged elastic band method for finding saddle points and minimum energy paths, J. Chem. Phys. 113 (22) (2000) 9901–9904.

[48] V. Wang, N. Xu, J.-C. Liu, G. Tang, W.-T. Geng, VASPKIT: a user-friendly interface facilitating high-throughput computing and analysis using VASP code, Comput. Phys. Commun. (2021) 108033.

[49] L. Barnard, D. Morgan, *Ab initio* molecular dynamics simulation of interstitial diffusion in Ni–Cr alloys and implications for radiation induced segregation, J. Nucl. Mater. 449 (1–3) (2014) 225–233.

[50] A. Stukowski, Visualization and analysis of atomistic simulation data with OVITO–the open visualization tool, Modell. Simul. Mater. Sci. Eng. 18 (1) (2009) 015012.

[51] A. Tamm, A. Aabloo, M. Klintenberg, M. Stocks, A. Caro, Atomic-scale properties of Ni-based FCC ternary, and quaternary alloys, Acta Mater. 99 (2015) 307–312.

[52] W.K. Hastings, Monte Carlo sampling methods using Markov chains and their applications (1970).

[53] J. Cowley, An approximate theory of order in alloys, Phys. Rev. 77 (5) (1950) 669.

[54] J.F. Ziegler, M.D. Ziegler, J.P. Biersack, SRIM–the stopping and range of ions in matter (2010), Nucl. Instrum. Methods Phys. Res., Sect. B 268 (11–12) (2010) 1818–1823.

[55] G.S. Was, Fundamentals of Radiation Materials Science: Metals and Alloys, Springer, 2016.

[56] R.E. Stoller, M.B. Toloczko, G.S. Was, A.G. Certain, S. Dwaraknath, F.A. Garner, On the use of SRIM for computing radiation damage exposure, Nucl. Instrum. Methods Phys. Res. Sect. B 310 (2013) 75–80.

[57] C. Lu, K. Jin, L.K. Béland, F. Zhang, T. Yang, L. Qiao, Y. Zhang, H. Bei, H.M. Christen, R.E. Stoller, et al., Direct observation of defect range and evolution in ion-irradiated single crystalline Ni and Ni binary alloys, Sci. Rep. 6 (1) (2016) 1–10.

[58] D.B. Miracle, O.N. Senkov, A critical review of high entropy alloys and related concepts, Acta Mater. 122 (2017) 448–511.

[59] M.C. Gao, J.-W. Yeh, P.K. Liaw, Y. Zhang, et al., High-Entropy Alloys, Cham: Springer International Publishing, 2016.

[60] Z. Wang, W. Qiu, Y. Yang, C. Liu, Atomic-size and lattice-distortion effects in newly developed high-entropy alloys with multiple principal elements, Intermetallics 64 (2015) 63–69.

[61] H. Song, F. Tian, Q.-M. Hu, L. Vitos, Y. Wang, J. Shen, N. Chen, Local lattice distortion in high-entropy alloys, Phys. Rev. Mater. 1 (2) (2017) 023404.

[62] I.U. of Crystallography, C.H. Macgillavry, G.D. Rieck, K. Lonsdale, International Tables for X-ray Crystallography, Kynoch Press, 1962.

[63] Y. Zhang, Y.J. Zhou, J.P. Lin, G.L. Chen, P.K. Liaw, Solid-solution phase formation rules for multi-component alloys, Adv. Eng. Mater. 10 (6) (2008) 534–538.

[64] S. Guo, Q. Hu, C. Ng, C. Liu, More than entropy in high-entropy alloys: forming solid solutions or amorphous phase, Intermetallics 41 (2013) 96–103.

[65] S. Huang, Z. Dong, W. Mu, V. Ström, G. Chai, L. Vitos, Thermo-elastic properties of bcc Mn-rich high-entropy alloy, Appl. Phys. Lett. 117 (16) (2020) 164101.

[66] G. Grad, P. Blaha, J. Luitz, K. Schwarz, A.F. Guillermet, S. Sferco, Electronic structure and chemical bonding effects upon the bcc to ω phase transition: ab initio study of y, zr, nb, and mo, Phys. Rev. B 62 (19) (2000) 12743.

[67] G.D. Samolyuk, Y. Osetsky, G.M. Stocks, J. Morris, Role of static displacements in stabilizing body centered cubic high entropy alloys, Phys. Rev. Lett. 126 (2) (2021) 025501.

[68] Y. Ikeda, K. Gubaev, J. Neugebauer, B. Grabowski, F. Körmann, Chemically induced local lattice distortions versus structural phase transformations in compositionally complex alloys, npj Comput. Mater. 7 (1) (2021) 1–8.

[69] P.K. Nandi, M. Valsakumar, S. Chandra, H. Sahu, C. Sundar, Efficacy of surface error corrections to density functional theory calculations of vacancy formation energy in transition metals, J. Phys. 22 (34) (2010) 345501.

[70] Y. Gong, B. Grabowski, A. Glensk, F. Körmann, J. Neugebauer, R.C. Reed, Temperature dependence of the Gibbs energy of vacancy formation of fcc Ni, Phys. Rev. B 97 (21) (2018) 214106.

[71] A. Schneider, C.-C. Fu, C. Barreteau, Local environment dependence of Mn magnetism in bcc iron-manganese alloys: a first-principles study, Phys. Rev. B 98 (9) (2018) 094426.

[72] J. Burton, Vacancy-formation entropy in cubic metals, Phys. Rev. B 5 (8) (1972) 2948.

[73] X. Zhang, M.H. Sluiter, Ab initio prediction of vacancy properties in concentrated alloys: the case of fcc Cu-Ni, Phys. Rev. B 91 (17) (2015) 174107.

[74] B. Grabowski, Y. Ikeda, P. Srinivasan, F. Körmann, C. Freysoldt, A.I. Duff, A. Shapeev, J. Neugebauer, Ab initio vibrational free energies including anharmonicity for multicomponent alloys, npj Comput. Mater. 5 (1) (2019) 1–6.

[75] X. Zhang, B. Grabowski, F. Körmann, C. Freysoldt, J. Neugebauer, Accurate electronic free energies of the 3D, 4D, and 5D transition metals at high temperatures, Phys. Rev. B 95 (16) (2017) 165126.

[76] X. Zhang, B. Grabowski, T. Hickel, J. Neugebauer, Calculating free energies of point defects from *ab initio*, Comput. Mater. Sci 148 (2018) 249–259.

[77] A. Manzoor, S. Pandey, D. Chakraborty, S.R. Phillpot, D.S. Aidhy, Entropy contributions to phase stability in binary random solid solutions, npj Comput. Mater. 4 (1) (2018) 1–10.

[78] Y. Zhang, K. Jin, H. Xue, C. Lu, R.J. Olsen, L.K. Beland, M.W. Ullah, S. Zhao, H. Bei, D.S. Aidhy, et al., Influence of chemical disorder on energy dissipation and defect evolution in advanced alloys, J. Mater. Res. 31 (16) (2016) 2363–2375.

[79] R. LeSar, Introduction to Computational Materials Science: Fundamentals to Applications, Cambridge University Press, 2013.

[80] G.D. Samolyuk, A.V. Barashev, S.I. Golubov, Y. Osetsky, R.E. Stoller, Analysis of the anisotropy of point defect diffusion in hcp Zr, Acta Mater. 78 (2014) 173–180.

[81] S. Shang, L. Hector Jr, Y. Wang, Z. Liu, Anomalous energy pathway of vacancy migration and self-diffusion in hcp Ti, Phys. Rev. B 83 (22) (2011) 224104.

[82] F. Willaime, Ab initio study of self-interstitials in hcp-Zr, J. Nucl. Mater. 323 (2–3) (2003) 205–212.

[83] B. Eyre, R. Bullough, On the formation of interstitial loops in bcc metals, Philos. Mag. 12 (115) (1965) 31–39.

[84] B. Wirth, G. Odette, D. Maroudas, G. Lucas, Dislocation loop structure, energy and mobility of self-interstitial atom clusters in bcc iron, J. Nucl. Mater. 276 (1–3) (2000) 33–40.

[85] J. Chen, N. Gao, P. Jung, T. Sauvage, A new mechanism of loop formation and transformation in bcc iron without dislocation reaction, J. Nucl. Mater. 441 (1–3) (2013) 216–221.

[86] Y. Zhang, Z. Xiao, X.-M. Bai, Effect of Cr concentration on 1/2<111> to <100> dislocation loop transformation in Fe-Cr alloys, J. Nucl. Mater. 543 (2021) 152592.

[87] J. Kärger, D.M. Ruthven, Diffusion in Zeolites and Other Microporous Solids, Wiley New York, 1992.

[88] N. Anento, A. Serra, Y.N. Osetsky, Atomistic study of multimechanism diffusion by self-interstitial defects in α-Fe, Modell. Simul. Mater. Sci. Eng. 18 (2) (2010) 025008.

[89] H. Wiedersich, P. Okamoto, N.Q. Lam, A theory of radiation-induced segregation in concentrated alloys, J. Nucl. Mater. 83 (1) (1979) 98–108.

[90] A. Marwick, Segregation in irradiated alloys: the inverse Kirkendall effect and the effect of constitution on void swelling, J. Phys. F 8 (9) (1978) 1849.

[91] T. Allen, J. Busby, G. Was, E. Kenik, On the mechanism of radiation-induced segregation in austenitic Fe–Cr–Ni alloys, J. Nucl. Mater. 255 (1) (1998) 44–58.

[92] P. Okamoto, L. Rehn, Radiation-induced segregation in binary and ternary alloys, J. Nucl. Mater. 83 (1) (1979) 2–23.

[93] B. Loomis, A. Taylor, S. Gerber, Void swelling of Nb and Nb-1% Zr induced by 58Ni+ bombardment, J. Nucl. Mater. 56 (1) (1975) 25–37.

[94] B. Loomis, S. Gerber, A. Taylor, Void ordering in ion-irradiated Nb and Nb-1% Zr, J. Nucl. Mater. 68 (1) (1977) 19–31.

[95] N. Ghoniem, D. Walgraef, S. Zinkle, Theory and experiment of nanostructure self-organization in irradiated materials, J. Comput.-Aided Mater. Des. 8 (1) (2001) 1–38.

[96] J.L. Brimhall, G.L. Kulcinski, Void formation in ion bombarded niobium, Radiat. Eff. 20 (1–2) (1973) 25–31.

[97] B. Loomis, S. Gerber, Void formation and solute segregation in ion-irradiated niobium-base alloys, J. Nucl. Mater. 117 (1983) 224–233.

[98] Y. Lederer, C. Toher, K.S. Vecchio, S. Curtarolo, The search for high entropy alloys: a high-throughput *ab-initio* approach, Acta Mater. 159 (2018) 364–383.

[99] Q. Ding, Y. Zhang, X. Chen, X. Fu, D. Chen, S. Chen, L. Gu, F. Wei, H. Bei, Y. Gao, et al., Tuning element distribution, structure and properties by composition in high-entropy alloys, Nature 574 (7777) (2019) 223–227.

[100] X. Chen, Q. Wang, Z. Cheng, M. Zhu, H. Zhou, P. Jiang, L. Zhou, Q. Xue, F. Yuan, J. Zhu, et al., Direct observation of chemical short-range order in a medium-entropy alloy, Nature 592 (7856) (2021) 712–716.

[101] R. Zhang, S. Zhao, J. Ding, Y. Chong, T. Jia, C. Ophus, M. Asta, R.O. Ritchie, A.M. Minor, Short-range order and its impact on the CrCoNi medium-entropy alloy, Nature 581 (7808) (2020) 283–287.

[102] S. Zhao, Local ordering tendency in body-centered cubic (BCC) multi-principal element alloys, J. Phase Equilib. Diffus. (2021) 1–14.

[103] X. Zhou, H. Wadley, R.A. Johnson, D. Larson, N. Tabat, A. Cerezo, A. Petford–Long, G. Smith, P. Clifton, R. Martens, et al., Atomic scale structure of sputtered metal multilayers, Acta Mater. 49 (19) (2001) 4005–4015.

[104] D.-Y. Lin, S. Wang, D. Peng, M. Li, X. Hui, An n-body potential for a Zr–Nb system based on the embedded-atom method, J. Phys. 25 (10) (2013) 105404.